

On the detectability of higher harmonics with LISA

Chantal Pitte,^{1,*} Quentin Baghi,¹ Sylvain Marsat,² Marc Besançon,¹ and Antoine Petiteau^{1,3}

¹*IRFU, CEA, Université Paris-Saclay, F-91191, Gif-sur-Yvette, France.*

²*Laboratoire des 2 Infinis - Toulouse (L2IT-IN2P3),*

Université de Toulouse, CNRS, UPS, F-31062 Toulouse Cedex 9, France.

³*Astroparticule et Cosmologie, Université de Paris, CNRS, Paris, 75013, France*

(Dated: April 7, 2023)

Supermassive black hole binaries (SMBHB) are expected to be detected by the future space-based gravitational-wave detector LISA with a large signal-to-noise ratio (SNR). This prospect enhances the possibility of differentiating higher harmonics in the inspiral-merger-ringdown (IMR) waveform. In this study, we test the ability of LISA to identify the presence of different modes in the IMR waveform from a SMBHB. We analyze the contribution of each mode to the total SNR for different sources. We show that higher modes, in particular, the mode (3, 3) and (4, 4), can dominate the signal observed through the LISA detector for SMBHB of the order of $10^8 M_\odot$. With Bayesian analysis, we can discriminate models with different IMR modes. While higher modes are often considered to be orthogonal, it is no longer the case in the merger-ringdown phase. Therefore, omitting harmonics not only diminishes the SNR but can also lead to biases in the parameter estimation. We analyze the bias for each model for our example system and quantify the threshold SNR where we can expect the parameter bias to be comparable to the statistical error. Our work highlights the importance of higher modes to describe the gravitational waveform of events detected by LISA.

I. INTRODUCTION

In the next decade, the Laser Interferometer Space Antenna (LISA) [1, 2] will leave Earth on the quest to find new gravitational waves (GW) sources. The most intense signals are expected to come from the coalescence of supermassive black holes binaries (SMBHB), whose predicted rate depends on the population and evolution model [3]. We can approximate this rate to be of the order of 1-100 per year with a signal-to-noise ratio (SNR) ranging from a few tens up to thousands [4]. These high-SNR sources bring hope to test general relativity (GR). One way to put Einstein's theory to the test with black hole binary's (BHB) coalescence is to probe the No-hair theorem [5] through the study quasi-normal modes (QNM) [6].

After two compact objects have merged into one, a final black hole (BH) in a perturbed state is expected to be obtained. As it stabilizes to quiescence (ring-down regime), it will emit gravitational radiation that can be described as a superposition of sinusoidal oscillations decaying over time, namely the QNMs [7–10]. Each QNM has an associated complex frequency, labeled by (l, m, n) as polar, azimuthal and overtone indices respectively. In GR these solutions are completely determined by the final black hole's mass and spin (M_f, a_f) [11, 12]. Nonetheless, the corresponding amplitude and phase are modulated by characteristics from the progenitors (initial BHs), as well as their relative orientation towards the observer [13, 14]. The eigen-functions of the ringdown, the spin-weighted 'spheroidal' harmonics, can be projected

into spin-weighted spherical harmonics, basis of numerical relativity (NR) (see Eq. (3.7) in [7], also see [15–17] for further information and mixing of the modes). A motivation for this representation, besides the orthogonality of the second group, is that it is the one conventionally used to describe the full inspiral-merger-ringdown (IMR) waveform, as it is done for instance in phenomenological models, where only the fundamental QNM $(l, m, n=0)$ is included in the ringdown. From now on, we will refer to spin-weighted spherical harmonics components of the IMR waveform, indexed by their mode numbers (l, m) , as *modes*. The response of LISA can be included as a transfer function in frequency domain separately for each mode, the same domain in which IMR phenomenological models work [18–20], allowing us to produce fast IMR waveforms with the appropriate instrumental response [21].

Investigating the role of higher harmonics in SMBHB signals is important because of the high SNR that these events will have in LISA. The analysis of such strong signals will be sensitive to many subdominant features in the waveforms, and in particular to the higher harmonics beyond the dominant (2, 2) mode. Modes with different 'm' are often considered to be orthogonal, since their phases scale differently with the orbital phase as $m\phi_{\text{orb}}$, leading to destructive interference. This is true for the inspiral, but we will show that this no longer holds for the merger-ringdown phase where a large SNR is accumulated over only few wave cycles. When performing parameter estimation, the contribution of cross terms to the likelihood translates not only to SNR contribution, but also into bias in the parameter inference if certain modes are ignored.

The correct estimation of the parameters of the full waveform is crucial in particular for tests of the No-hair

* chantal.pitte@cea.fr

theorem. There are two main approaches to probe the No-hair hypothesis. The first one uses two QNM parameters to find the ‘hairs’ of the final BH, i.e. final mass and spin (M_f, a_f) , while a third QNM parameter, or preferably more, are used to check for consistency [6, 22]. The second approach compares the estimated final parameters from the full IMR or pre-merger waveform, with those obtained from only the ringdown [23], looking for possible deviations from GR. Note that in the latter case, the measure of only one harmonic is necessary to test the hypothesis. A third method called the ‘merger-ringdown’ test has recently been proposed to check for consistency between both regimes. It is based on the relation of the amplitude and the phase of the QNMs with respect to properties of the progenitors [24]. Naturally, to test the hypothesis with any method, one should know with high accuracy and precision the intrinsic parameters: total mass M and mass ratio q of the initial BHs, as well as individuals spins S_i for the case of spinning systems. Given their analytical relation to the final BH (see e.g. [18, 25]), one can obtain the values of final mass and spin (M_f, a_f) to do BH’s spectroscopy (study of the BH’s harmonics). Nonetheless, one should also know the extrinsic parameters to analyse the ringdown regime, either from the IMR or pre-merger inference.

Several analyses of black hole spectroscopy have been proposed over the years [12, 26–30]. Regarding the first No-hair theorem test method, the work from [22] was the first to use Bayesian analysis to study deviations from GR, nonetheless see [31, 32]. Concerning the second approach, studies of the detectability of overtones ($n \geq 1$) or higher angular modes ($l, m \geq 2$) have been performed. The LIGO-Virgo-Kagra (LVK) collaboration as well as other authors [23, 33–38] conducted analysis on the presence of higher modes for the detected event GW150914 [39]. Tension between the results of these authors is observed. We can also remark [40], where the pEOBNR formalism (full IMR waveform) was used to study possible deviations from GR for events-like in LVK. To this date and to our knowledge, the full response of LISA (including high-frequency effects) has not been taken into account to study ringdown signals.

In this study we evaluate our ability to identify and differentiate modes of a plausible source detected by LISA, and investigate the possible consequences of mismodeling these modes. To this end, we make use of the software `lisabeta` [41], which incorporates LISA’s response into the source waveform, as described in Section II. We continue with the explanation of the study methodology in Section III. In Section IV we analyze the contribution of the modes to the total SNR for general cases. Then we focus our attention on the impact of these contributions onto the estimation of parameters for a specific event in Section V. In that section we also analyze the errors produced by the use of an incorrect template relative to the source SNR. Finally, we summarize our conclusions in Section VI.

II. SUPERMASSIVE BLACK HOLE WAVEFORMS IN LISA

To study signals observed by LISA we need to incorporate its instrumental response to the GW signature produced by an event. We use the `lisabeta` software developed for this purpose, which takes into account several effects from LISA’s instrument. We review the main features implemented in `lisabeta` that are of particular interest for our study in the following subsections. More detailed information can be found in [21].

A. Waveform in the source and detector frames

For our study we generate the SMBHB waveform with PhenomHM [20], which is a phenomenological method based on PhenomD [18, 19] for non-precessing binaries. In addition to the dominant quadrupole ($l = 2, m = 2$), higher modes are introduced, including $(l, m) = (2, 1), (3, 3), (3, 2), (4, 4), (4, 3)$. Incorporating these higher modes brings crucial complementary information, not only in the ringdown part of the signal, but also in the inspiral and merger, which has been shown to narrow the posterior of extrinsic parameters down in the inference [42, 43].

The gravitational wave signal can be decomposed in spin-weighted spherical harmonics ${}_{-2}Y_{lm}$, which depend on the orientation of emission parametrized by the inclination ι and the phase φ . The polarizations h_+ and h_\times of a GW are related to their harmonics by

$$h_+ - ih_\times = \sum_{l \geq 2} \sum_{m=-l}^l {}_{-2}Y_{lm}(\iota, \varphi) h_{lm}, \quad (1)$$

where each mode can be described in terms of an amplitude A_{lm} and a phase Φ_{lm} that depend on intrinsic parameters

$$h_{lm} = A_{lm} e^{-i\Phi_{lm}}. \quad (2)$$

In the frequency domain, non-precessing binary systems have an advantageous symmetry relation between progrades and retrogrades modes (m and $-m$). It allows us to describe each polarization as

$$\tilde{h}_{+, \times}(f) = \sum_l \sum_{m > 0} K_{lm}^{+, \times} \tilde{h}_{lm}(f), \quad (3)$$

where we introduced

$$K_{lm}^+ = \frac{1}{2} (-2Y_{lm} + (-1)^l {}_{-2}Y_{l-m}^*), \quad (4a)$$

$$K_{lm}^\times = \frac{i}{2} (-2Y_{lm} - (-1)^l {}_{-2}Y_{l-m}^*). \quad (4b)$$

The GW strain in the traceless-transverse gauge is expressed as

$$h^{TT} = \mathbf{e}_+ h_+ + \mathbf{e}_\times h_\times, \quad (5)$$

where $\mathbf{e}_{+,\times}$ are the polarization tensors,

$$\mathbf{e}_+ = \mathbf{u} \otimes \mathbf{u} - \mathbf{v} \otimes \mathbf{v}, \quad (6a)$$

$$\mathbf{e}_\times = \mathbf{u} \otimes \mathbf{v} + \mathbf{v} \otimes \mathbf{u}. \quad (6b)$$

Vectors \mathbf{v} and \mathbf{u} together with the propagation vector \mathbf{k} in spherical coordinates locate the source in the observational frame,

$$\mathbf{u} = \{\sin \lambda, \cos \lambda, 0\}, \quad (7a)$$

$$\mathbf{v} = \{-\sin \beta \cos \lambda, -\sin \beta \sin \lambda, \cos \beta\}, \quad (7b)$$

$$\mathbf{k} = \{-\cos \beta \cos \lambda, -\cos \beta \sin \lambda, -\sin \beta\}. \quad (7c)$$

with (β, λ) as the ecliptic latitude and longitude.

Combining previous equations, we obtain a final expression

$$\tilde{h}^{TT}(f) = \sum_{l,m} P_{lm} \tilde{h}_{lm}(f), \quad (8)$$

where

$$\begin{aligned} P_{lm} &= \mathbf{e}_+ K_{lm}^+ + \mathbf{e}_\times K_{lm}^\times \\ &= \frac{1}{2} \left[{}_{-2}Y_{lm}(\mathbf{e}_+ + i \mathbf{e}_\times) e^{-2i\psi} \right. \\ &\quad \left. + (-1)^l {}_{-2}Y_{l-m}^*(\mathbf{e}_+ - i \mathbf{e}_\times) e^{2i\psi} \right]. \end{aligned} \quad (9)$$

Note that P_{lm} depends not only on (l, m) and (ι, φ) from the spherical harmonics, but also on the parameters defining the reference frame, such as the sky localization (β, λ) and the polarization ψ .

B. LISA response

The LISA constellation is composed by three spacecrafts (S/C) deployed in a triangular shape. As a GW travels across one arm of the constellation, the detectors at both ends of the arm will read the frequency shift between the sent and received signals. This response is known as the link response. One advantage of this setup is that it allows for multiple interferometers with different combinations of the links. Each link response is defined as

$$\begin{aligned} y_{rs}(t_r) &\simeq \frac{1}{2 \left(1 - \hat{\mathbf{k}} \cdot \hat{\mathbf{n}}_{rs}(t_r) \right)} \left[H_{rs}(t_r - L_{rs}(t_r) - \right. \\ &\quad \left. \hat{\mathbf{k}} \cdot \mathbf{x}_r(t_r) \right) - H_{rs}(t_r - \hat{\mathbf{k}} \cdot \mathbf{x}_s(t_r)) \Big], \end{aligned} \quad (10)$$

where we used $c = 1$. The position of the S/C is designated by $\mathbf{x}_{r,s}$ and the sub-indices s stands for sender, while r stands for receiver. Note the ordering of those indices which follows the last convention adopted in [44]. Their values go from 1 to 3, indexing the 3 S/C. Therefore 6 combinations are produced, resulting in 6 different links. The unit vector $\hat{\mathbf{k}}$ defines the direction of propagation of the GW, while $\hat{\mathbf{n}}_{rs}$ is the direction of the beam.

Finally, L_{rs} is the arm's length between the two S/C and H_{rs} is the projected gravitational strain produced by the source,

$$\begin{aligned} H_{rs}(t) &= (h_+(t) \cos 2\psi - \\ &\quad h_\times(t) \sin 2\psi) \hat{\mathbf{n}}_{rs}(t) \cdot \mathbf{e}_+ \cdot \hat{\mathbf{n}}_{rs}(t) \\ &\quad + (h_+(t) \sin 2\psi + \\ &\quad h_\times(t) \cos 2\psi) \hat{\mathbf{n}}_{rs}(t) \cdot \mathbf{e}_\times \cdot \hat{\mathbf{n}}_{rs}(t). \end{aligned} \quad (11)$$

The constellation as a whole will follow Earth in the same orbit, however each S/C will have a defined orbit around the sun and thus within the constellation. This translates into a time variation in the orientation of the detector with respect to the solar system barycenter frame (SSB). Note that this introduces modulations on the signal observed by LISA, as is noticeable from the explicit time-dependent prefactors and delays in the instrumental response given by Eqs. (10) and (11). In LISA's frequency band, the observation of one event can last from days to years, prone to be strongly affected by these modulations. Additionally, in the post-processing, beams are combined in the time-delay interferometry (TDI, see Ref. [45, 46] and Sec. II B 1) to cancel laser frequency noise, so that time delays and changes in those delays leave an imprint in the measured signal.

1. TDI and frequency domain formulation

Time delay interferometry was first proposed by Armstrong, Estabrook and Tinto [47] as a solution to cancel the dominant noise produced by fluctuations in the laser frequency. The idea is to combine the links linearly with the adequate time delay to eliminate the laser noise. Different combinations have been proposed depending on the characteristics on the constellation. We can find what is known as first-generation Michelson interferometer (TDI 1.5) for a stationary unequal-arm constellation, and second-generation Michelson interferometry (TDI 2.0) for a rotating unequal- and flexing-arm constellation. Note that any real constellation will have flexing arms, which prompted the development of TDI 2.0.

It was shown (see e.g. [21]) that it is possible to approximately express the response of the links in terms of the harmonics in frequency domain as

$$\tilde{y}_{rs}(f) = \sum_{lm} \mathcal{T}_{rs}^{lm}(f) \tilde{h}_{lm}(f), \quad (12)$$

where $\mathcal{T}_{rs}^{lm}(f) = G_{rs}^{lm}(f, t_f^{lm})$ is a kernel carrying information on the modulation and time-delay of the links response. It is defined as

$$\begin{aligned} G_{rs}^{lm}(f, t) &= \frac{i\pi f L_{rs}}{2} \text{sinc} \left[\pi f L_{rs} \left(1 - \hat{\mathbf{k}} \cdot \hat{\mathbf{n}}_{rs}(t) \right) \right] \\ &\quad e^{i\pi f (L_{rs} + \hat{\mathbf{k}} \cdot [\mathbf{x}_r(t) + \mathbf{x}_s(t)])} \hat{\mathbf{n}}_{rs}(t) \cdot P_{lm} \cdot \hat{\mathbf{n}}_{rs}(t). \end{aligned} \quad (13)$$

The frequency-domain response can then be obtained thanks to a generalized relation giving a time-to-frequency correspondence. This relation extends the one found within the stationary phase approximation (SPA) [48, 49], that applies only to the slowly evolving inspiral signal, to the merger-ringdown part of the signal. It reads [21, 42]

$$t_f^{lm} \equiv -\frac{1}{2\pi} \frac{d\Phi^{lm}}{df}. \quad (14)$$

To simplify the transfer function in frequency domain, some assumptions were made:

- the constellation forms an equilateral triangle, then the arms will remain equal and constant;
- $L_{12} = L_{21}$, i.e. the arm's length is similar in both directions since the relative motion of the beam relative to the S/C (also known as pointing-ahead effect) is not taken into account.

With these assumptions and after factoring out several terms, we can write the response in terms of channels A, E, T ; the optimal linear combinations of Michelson variables [50] that are approximately orthogonal relative to the noise. They read

$$\tilde{A} = \frac{i\sqrt{2}\sin(2\pi fL)}{e^{-2i\pi fL}} [(1+z)(\tilde{y}_{13} + \tilde{y}_{31}) - \tilde{y}_{32} - z\tilde{y}_{23} - \tilde{y}_{12} - z\tilde{y}_{21}], \quad (15a)$$

$$\tilde{E} = \frac{i\sqrt{2}\sin(2\pi fL)}{\sqrt{3}e^{-2i\pi fL}} [(1-z)(\tilde{y}_{31} + \tilde{y}_{13}) + (2+z)(\tilde{y}_{21} - \tilde{y}_{23}) + (1+2z)(\tilde{y}_{12} - \tilde{y}_{32})], \quad (15b)$$

$$\tilde{T} = \frac{4\sin(\pi fL)\sin(2\pi fL)}{\sqrt{3}e^{-3i\pi fL}} [\tilde{y}_{12} - \tilde{y}_{21} + \tilde{y}_{23} - \tilde{y}_{32} + \tilde{y}_{31} - \tilde{y}_{13}], \quad (15c)$$

with $z \equiv e^{2i\pi fL}$.

III. METHODOLOGY

The goal of this study is to quantify our ability to identify the presence of different modes in a SMBHB event detected by LISA. We expect the detectability of the modes to be not only related to the value of the SNR itself, but also to the relative SNR of each mode. In this framework there are two main parameters to consider in the computation of the SNR: the luminosity distance and the mass. While the distance is just a scaling factor that will affect all modes in similar manner, the mass, and therefore the frequency, has a strong effect in moving the signal to lower and higher frequencies and deciding the relative weight of the inspiral and merger-ringdown. Since the observed signal is characterized by a redshifted mass, we will distinguish between the source-frame mass and the observed (redshifted) mass.

As an analogy to the luminosity peak in time domain, we use here an ad-hoc frequency domain definition of *frequency peak* as the frequency at the maximum value of the observed re-scaled TDI variable for each mode; see Eq. (29) of [42] for a definition of re-scaled TDI variables. With the time-to-frequency correspondence in Eq. (14), this parameter lays about $2.4t_M$ ($t_M = tc^3/MG$, adimensional value) after the time of coalescence. In the waveform observed by LISA, this frequency peak roughly represents the beginning of the ringdown regime, even though there is no clear starting point for it (see ongoing discussion on this topic [16, 30, 51, 52]). The mass of the source will move the frequency peaks through the spectrum, so that the contribution of each mode depends on the sensitivity of LISA at the frequency peaks. For this reason we study the contribution of each mode in terms of the mass. Results are shown in Section IV.

Once we know the contribution of different modes in the general case, we can focus on a specific event as an example. The method we use to assess the detectability of modes is through parameter estimation with different models in a Bayesian analysis. Each model corresponds to a different combination of modes in the generation of the waveform. This method allows us to compare different models based on Bayes factors, as we shall see.

A. Bayesian analysis

In Bayesian analysis, the posterior distribution of the strain's parameters θ given the observed data d , is expressed as

$$p(\theta|d, M) = \frac{p(d|\theta, M)p(\theta|M)}{p(d|M)}, \quad (16)$$

where θ are the physical parameters of the source, M is the model (and any other context) considered, $p(d|M)$ is the evidence, $p(\theta|M)$ the prior of the parameters (in practice independent of M), and $p(d|\theta, M)$ the likelihood. The three latter are also usually denoted by \mathcal{Z} , $\pi(\theta)$ and $\mathcal{L}(\theta)$, as the evidence, the prior and the likelihood respectively. In the following we drop the indication of the model M in the equations.

The likelihood for a Gaussian noise with a covariance matrix \mathbf{C} takes the form

$$\mathcal{L} = \frac{1}{\sqrt{\det(2\pi\mathbf{C})}} e^{-\frac{1}{2}(d-h(\theta))^\dagger \mathbf{C}^{-1}(d-h(\theta))}. \quad (17)$$

From now on we drop the tilde notation for simplicity, even though we work in frequency domain. One advantage of working in the frequency domain is that when dealing with stationary noise, each frequency bin is approximately independent. The noise covariance can therefore be diagonalized and represented by its power spectral density (PSD).

We introduce the definition of the inner product as

$$(a|b) = 4\text{Re} \int_0^\infty \frac{a(f)b^*(f)}{S_n(f)} df, \quad (18)$$

where S_n is the noise's PSD and the star (*) is the complex conjugate. Eq. (17) can thus be rewritten as

$$\ln \mathcal{L} = -\frac{1}{2}(d - h(\boldsymbol{\theta})|d - h(\boldsymbol{\theta})) + \text{const.} \quad (19)$$

It can be decomposed as

$$\ln \mathcal{L} = (d|h(\boldsymbol{\theta})) - \frac{1}{2}(h(\boldsymbol{\theta})|h(\boldsymbol{\theta})) - \frac{1}{2}(d|d), \quad (20)$$

where the last term can be neglected, since it does not depend on the estimated parameters and represents a multiplicative constant in the likelihood. When combining different independent instrumental channels such as A, E, T , the log-likelihood is simply written as a sum over these channels. To speed up the computation of the likelihood, we use an adaptative heterodyned likelihood (see [53, 54] and references therein for more information).

Given a chosen prior, the Bayes factor is a mean to compute the preference of the data towards one model or another. It is defined as the ratio of the evidences \mathcal{Z} of two models i and j

$$\mathcal{B} = \frac{\mathcal{Z}_i}{\mathcal{Z}_j}, \quad (21)$$

where the evidence is the integral of the likelihood over the whole parameter's hyper-volume,

$$\mathcal{Z} = \int_{\Theta} \mathcal{L}(\theta) \pi(\theta) d\theta. \quad (22)$$

IV. STUDY OF THE MODES CONTRIBUTIONS TO THE SNR

The SNR builds up in time and in frequency, and is defined by ρ as

$$\rho^2 = \sum_{lm} \sum_{l'm'} \sum_{ch} 4 \text{Re} \int \frac{\mathcal{H}_{lm}^{ch}(f) \mathcal{H}_{l'm'}^{ch*}(f)}{S_n(f)} df, \quad (23)$$

where the sum over independent channels (index ch) extends over A, E (which have the same noise PSD S_n). The assumed PSD is drawn from the 'science requirement model' SciRDv1 [2] including the galactic white dwarf confusion noise, with the subtractions of sources over 1 year. Note that we are using \mathcal{H}_{lm}^{ch} instead of h_{lm} . This is because we are also including LISA instrumental response and TDI post-processing combining Eqs. (12)

TABLE I: Source parameters in SSB frame with aligned spins and redshifted masses.

Parameter	Value	Parameter	Value
Mass (M_{\odot})	$[10^5, 5 \times 10^9]$	β (rad)	$\pi/2$
q (Mass ratio)	2	λ (rad)	π
χ_1	0.5	ϕ (rad)	$\pi/2$
χ_2	0.5	ψ (rad)	$\pi/2$
redshift	3	ι (rad)	$\pi/3$

to (15). They read

$$\begin{aligned} \mathcal{H}_{lm}^a(f) &= h_{lm}(f) \cdot \frac{i\sqrt{2} \sin(2\pi fL)}{e^{-2i\pi fL}} \cdot \\ &[(1+z(f))(\mathcal{T}_{13}^{lm}(f) + \mathcal{T}_{31}^{lm}(f)) - \\ &\mathcal{T}_{32}^{lm}(f) - z(f)\mathcal{T}_{23}^{lm}(f) - \\ &\mathcal{T}_{12}^{lm}(f) - z(f)\mathcal{T}_{21}^{lm}(f)], \end{aligned} \quad (24a)$$

$$\begin{aligned} \mathcal{H}_{lm}^e(f) &= h_{lm}(f) \cdot \frac{i\sqrt{2} \sin(2\pi fL)}{\sqrt{3}e^{-2i\pi fL}} \cdot \\ &[(1-z(f))(\mathcal{T}_{31}^{lm}(f) + \mathcal{T}_{13}^{lm}(f)) + \\ &(2+z(f))(\mathcal{T}_{21}^{lm}(f) - \mathcal{T}_{23}^{lm}(f)) + \\ &(1+2z(f))(\mathcal{T}_{12}^{lm}(f) - \mathcal{T}_{32}^{lm}(f))], \end{aligned} \quad (24b)$$

where $z(f) = e^{2i\pi fL}$. For convenience we use the notation of inner product for modes,

$$(lm|l'm') = \sum_{ch} 4 \text{Re} \int \frac{\mathcal{H}_{lm}^{ch}(f) \mathcal{H}_{l'm'}^{ch*}(f)}{S_n(f)} df. \quad (25)$$

The the squared SNR can be written as

$$\rho^2 = \sum_{lm} \sum_{l'm'} (lm|l'm'). \quad (26)$$

Note that in Eq. (25), the cross terms $(lm|l'm')$ have no reason to be positive (> 0), and can contribute negatively to the total SNR. In other words, the phases can be constructive or destructive, which will depend on the values of the ecliptic latitude β and longitude λ , inclination ι , phase ϕ , polarization angle ψ and mass ratio q . An illustration of this outcome can be seen in Fig. 1. For this example, we use the parameters written in Table I with a redshifted mass of $\sim 2.44 \times 10^6 M_{\odot}$. In Fig. 1 we show the $(22|l'm')$ cross terms of the accumulated squared SNR (ρ^2) varying between positive and negative values depending on the frequency. After a certain point it remains constant, since there is no more contribution to the SNR, positive nor negative. This happens at a different frequency for each pair of modes. In dotted black line we plot the frequency peak of the $(2, 2)$ mode as a guide.

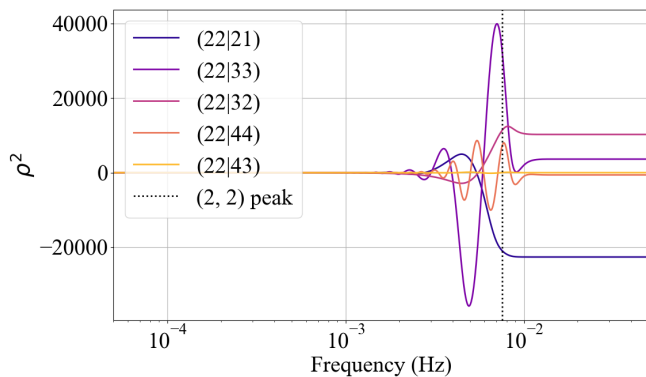


FIG. 1: Contribution of cross terms $(22|l'm')$ to ρ^2 . We can observe how the cumulative squared SNR changes from positive to negative values and vice-versa, until after the ringdown where it remains constant. The frequency peak of the mode $(2, 2)$ is shown here for guidance. Each mode peaks at a different frequency, so the stabilisation period starts at a different point for each pair of modes.

A. Dependency on mass and frequency

The next natural step to understand the detectability of modes is to analyze the contribution of each pairs of modes to the total SNR for different sources. As the SNR depends on each source's parameters, rather than attempting a full exploration of the parameter space or averaging over it, in the present study we simply fix all parameters but the mass to arbitrary values and normalize each contribution to the total SNR. Here again we chose the parameters listed in Table I. Note that the results, in particular the details of the hierarchy between modes and cross-terms, might depend on this choice of parameters.

We plot the results in Figs. 2a and 2b. The most observable feature is the positive contribution over all the frequencies of the square terms $(lm|lm)$, while cross terms $(lm|l'm')$ can have negative contributions as previously discussed. We decided to trace the frequency peak of the $(2, 2)$ mode (diagonal dotted line) as a mapping guide, since the contribution to the SNR changes considerably close to it. Depending on the mode, the variation will start before or after this frequency line. Note that each set of plots has its own colour bar. The numbers at the right of the bars represent the contribution ratio of each pair of modes to ρ^2 .

In the left plot of Fig. 2a, we note that the contribution of $(22|22)$ to ρ^2 is between 80% to 94% of the total, up to masses $\sim 4 \times 10^6 M_\odot$, while it decreases to 30% around masses of $\sim 10^8 M_\odot$. The rectangular darker area at the bottom right, between frequencies $[10^{-3} - 5 \times 10^{-2}]$ Hz and masses $[10^5 - 2 \times 10^6] M_\odot$, indicates that most of the SNR comes from the inspiral part. This is expected, since the waveform peaks outside or at the limit of the LISA frequency band. In contrast, the pair $(33|33)$ (in the cen-

tre) has a small contribution for low masses, but displays a considerable increase up to 21% for high masses around $10^8 M_\odot$. Finally, the case of $(44|44)$ (right plot) shows a similar behaviour but augmented by a factor ~ 2.5 , representing about 54% for large mass SMBHBs. In other words, if the redshifted total mass of the system is larger than $10^8 M_\odot$, the contribution of the quadrupolar mode will no longer predominate. It can represent half of the mode $(4, 4)$ and a factor 1.5 bigger than the mode $(3, 3)$. This highlights the importance of including higher harmonics to describe SMBHB signals.

The second set of plots in Fig. 2b shows the pairs of modes that make the highest contributions to the squared SNR, representing approximately from 1% to 5% of the total. This percentage might seem small, but for SMBHBs with a total SNR of 1000, the cross term's contribution can be of the order of 10 to 50. Those contributions are even higher than other square terms not shown here. We wanted to stress the possibility of a variable contribution during the merger-ringdown, that could remain negative at the last stage. Nonetheless, we use its absolute value to make the comparison of the contributions. The reason is that the sign depends on the extrinsic parameters and the mass ratio, which vary from source to source, but are fixed here to arbitrary values for the sake of illustration.

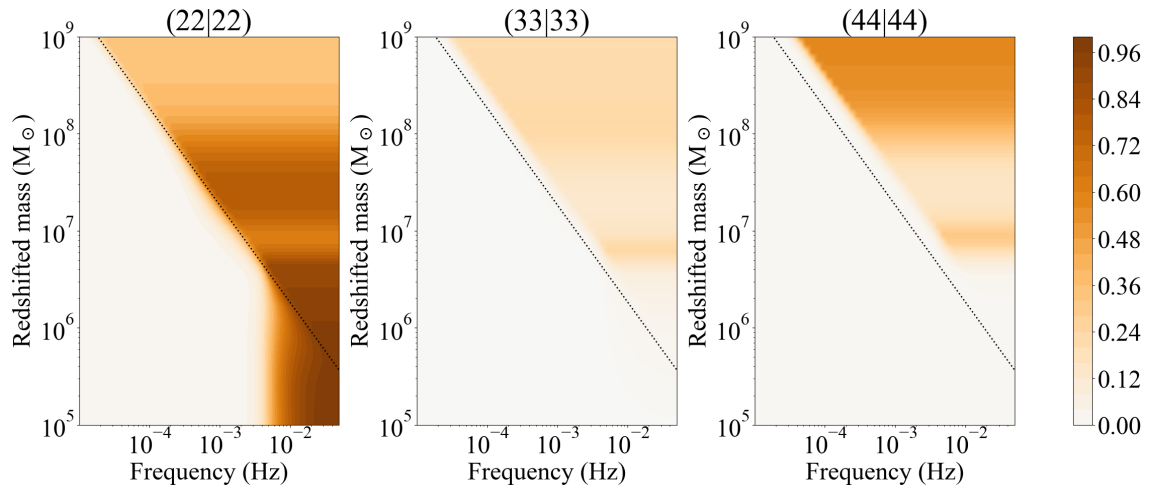
The position of the mode's frequency peak relative to the LISA sensitivity curve is driven by the event mass. Therefore, the SNR of higher modes can become more relevant than the $(2, 2)$ mode for large mass events.

B. Dependency on source mass and redshift

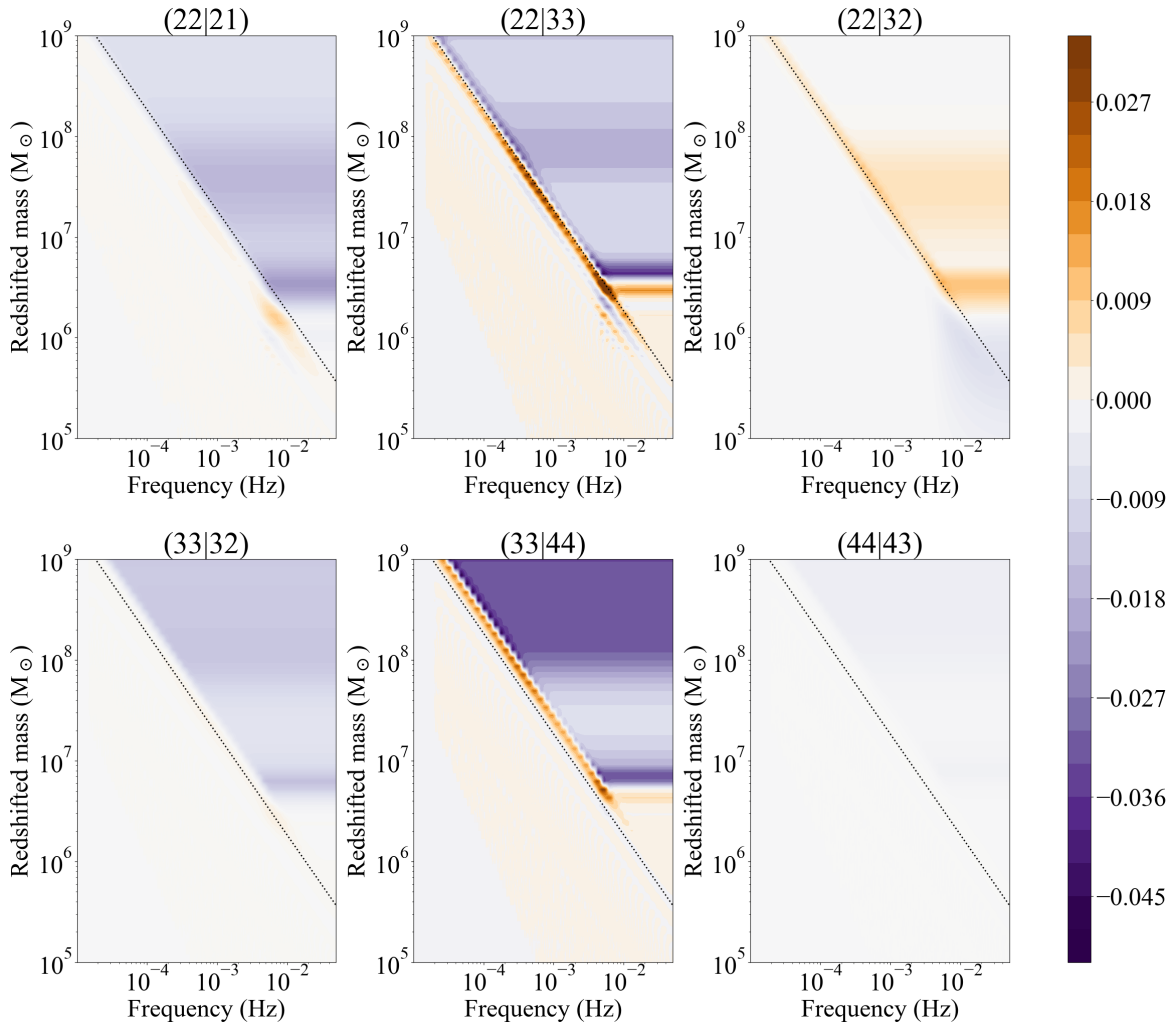
To represent the impact of the mass and the distance on the SNR, as mentioned in Section III, we show in Figs. 3a and 3b the contour plots for different modes depending on the total mass in the source frame. We choose to show the case of a source with parameters listed in Table I for the sake of an illustration, but of course the contributions would change with different parameters. Note that the lower bound of the total SNR is 10, which is the adopted threshold for SMBHB detection in LISA [1, 2].

In these figures, we can see the high contribution of the square terms $|(l, m = l|l, m = l)|^{1/2}$ as well as the highest-contributing cross terms such as $|(22|21)|^{1/2}$, $|(22|32)|^{1/2}$ and $|(33|32)|^{1/2}$. The complete array of pairs of modes is shown in Appendix A, Fig. 11.

The hierarchic relevance observed in Fig. 3a drove the motivation to include first the modes $(l, m = l)$ followed by $(l, m = l - 1)$ in ascendant l in the models definition in Section V A. The plot of the pairs $|(22|33)|^{1/2}$ and $|(22|32)|^{1/2}$ might call one's attention because of the zero contribution for systems with a total source mass around $10^6 M_\odot$. This effect can be explained by the chosen fixed parameters as previously mentioned. It is also visible in Fig. 1, where some values tend to a zero cumulative contribution, albeit their contribution in the merger and

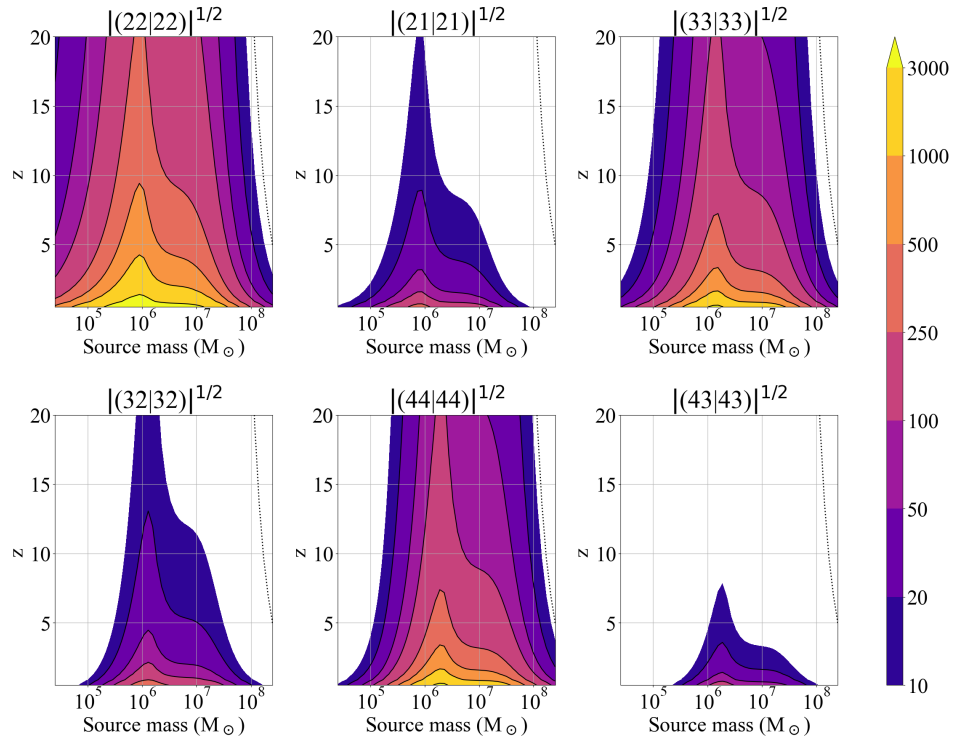


a) Ratio contribution of the square terms ($lm|lm$) to the total squared SNR.

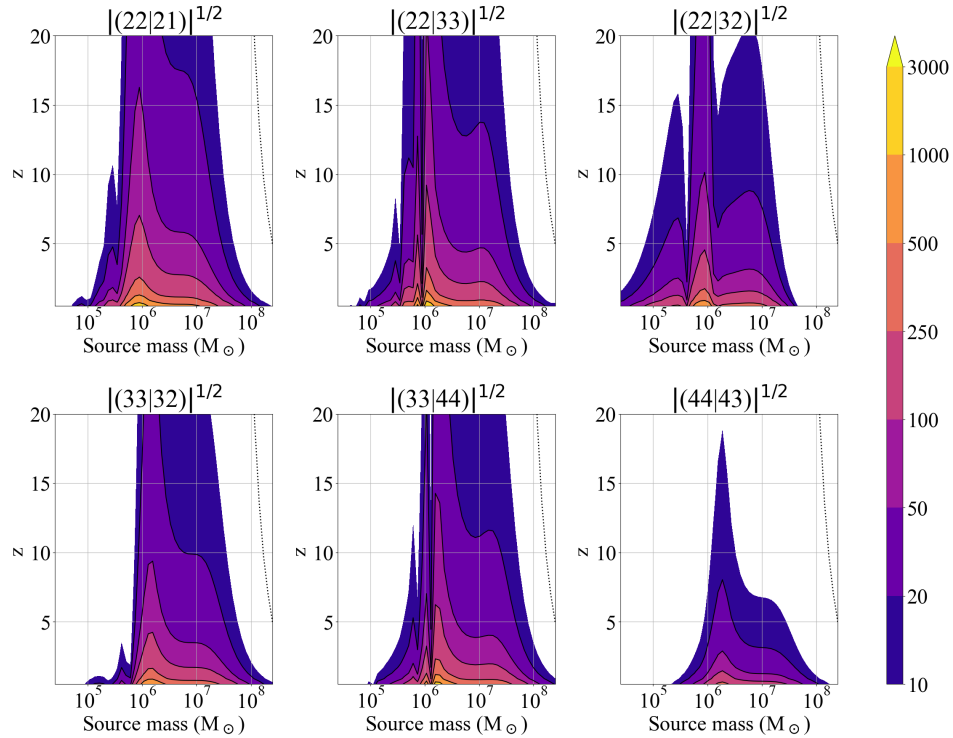


b) Highest ratio contributions of the cross terms ($lm|l'm'$) to the total squared SNR.

FIG. 2: Cumulative contribution to the squared SNR of pairs of modes depending on the total redshifted mass. In the top row we find the square terms with the largest ratios. The quadrupolar square term represents most of the contribution for low-mass sources, while it slowly decreases for more massive ones. The opposite happens for terms (33|33) and (44|44) albeit to a smaller extent. We show the cross terms in the last two rows. They oscillate between $\sim 1\%$ and 5% specially near the start of the ringdown, which is illustrated with a dotted line for the mode (2, 2) as a guidance. This percentage can represent a SNR of tens for a total SNR of thousands.



a) Contour plot with the contributions of square pairs of modes $|(lm|lm)|^{1/2}$.



b) Contour plot with the highest SNR contributions of cross terms $|(lm|l'm')|^{1/2}$.

FIG. 3: Contour plot for the root squared absolute cumulative value of contributions, namely $|(lm|l'm')|^{1/2}$. The dotted line correspond to the total SNR with a threshold of ≥ 10 , plotted here for comparison. We remark the sub-dominant contribution of $|(33|33)|^{1/2}$ and $|(44|44)|^{1/2}$ after the quadrupolar square term. Note the 0-contributions in some cross terms due to the representation of a single system with fixed parameters. The complete array for all contributions is plotted in Fig. 11

TABLE II: Parameters of the SMBHB source chosen from *Sangria*'s LDC catalogue for redshifted mass without precession. Interval for flat priors for the inference.

Parameter	Value	Prior
M_c (M_\odot)	857080.8396	$[10^4, 5 \times 10^7]$
q	2.7589	$[1, 10]$
χ_1	-0.5488	$[-1, 1]$
χ_2	0.2317	$[-1, 1]$
D_L (Mpc)	40084.6792	$[10^4, 5 \times 10^6]$
t_c (s)	0.0	$[-600, 600]$
β_L (rad)	-0.6186	$[-\pi/2, \pi/2]$
λ_L (rad)	2.2782	$[0, 2\pi]$
ϕ (rad)	0.2492	$[-\pi, \pi]$
Ψ_L (rad)	1.5158	$[0, \pi]$
ι (rad)	2.5969	$[0, \pi]$
SNR	744.36	

ringdown stage.

We also investigated the effect of the mass ratio by performing the same analysis, observing the SNR cancellation that was expected for equal mass systems (see A). Contour plots are shown in Fig. 10 in Appendix A.

V. EXAMPLE OF BAYESIAN ANALYSIS

A. Data and models

In order to understand the impact of higher modes in the parameter inference, we inject a SMBHB source signal with 6 modes. The parameters used to generate this source were taken from the LISA Data Challenges (LDC) *Sangria*'s catalogue [55], and detailed in Table II, where the subscript L in the extrinsic parameters means that it is expressed in the LISA frame at the time of coalescence t_c . Note also that we use the redshifted chirp mass M_c and mass ratio $q \geq 1$ instead of the individual masses. The parameters χ_i represent the aligned (non precessing binaries) BH's dimensionless spin, and D_L is the luminosity distance.

Two sets of data were considered, one without noise and another with noise. The noise was generated with the PSD assumed in Section IV. Each data set includes two TDI channels A and E . In both cases we restricted the frequency band to the interval $[10^{-5} - 5 \times 10^{-2}]$ Hz and ran a nested sampling algorithm to estimate the source parameters for various models. We chose the sampler `dynesty` [56], as it allows us to obtain approximate evidences (see Section III A and particularly Eq. 22). As a consistency check we also ran `ptemcee`, a parallel-tempered Markov Chain Monte Carlo ensemble sampler [57, 58]. We obtained consistent results with the two samplers, with a slightly better convergence for `ptemcee` (which does not allow for a direct computation of the evidence however). We report `dynesty` results in the following.

TABLE III: Each model is indexed according to number of modes included in the waveform generation.

Model	Modes (l,m)
M_1	(2, 2)
M_2	(2, 2), (3, 3)
M_3	(2, 2), (3, 3), (4, 4)
M_4	(2, 2), (3, 3), (4, 4), (2, 1)
M_5	(2, 2), (3, 3), (4, 4), (2, 1), (3, 2)
M_6	(2, 2), (3, 3), (4, 4), (2, 1), (3, 2), (4, 3)

We consider 6 models for the parameter estimation, where each one describes the waveform with a certain number of modes. The first model generates the gravitational signature with only the quadrupolar mode (2, 2). The other models include an increasing number of higher harmonics, ranked by their SNR contribution ($lm|lm$). This amounts to first selecting successive ($l, m = l$) modes with increasing l and then the ($l, m = l-1$) modes, as illustrated in Section IV B. See Table III for the definition of these models.

The priors we use are flat for all parameters in the intervals written in Table II, with the exception of the chirp mass which has a uniform prior in logarithmic scale. We use the whole physically allowed interval for the extrinsic parameters, while we use a raw estimation of the expected values for the intrinsic ones. For the time of coalescence we use a narrow prior as it can easily be spotted in the detection process, but with a difference up to 600 seconds between the LISA and the SSB reference frame. Note that the polarization ψ is allowed to go from 0 to π (and not 2π) to prevent degeneracy, given that in the antenna pattern the polarization is always preceded by a factor 2 as shown Eq.(9).

B. SNR and Bayes factor

Before presenting the Bayes factor and parameter estimation results, we can discuss our expectation regarding the contribution of modes. In our example, we consider a source event randomly chosen from the LDC *Sangria*'s catalogue with a SNR ~ 744 (see Table II). Converting the redshifted mass to the source-frame mass with a redshift of 4.3, we obtain the value of $2.28 \times 10^5 M_\odot$. Using Fig. 3, with this source-frame mass we can expect the term (22|22) to contribute the most whereas the rest of the SNR will come from (33|33) and (44|44) and from the cross terms (22|21) and (22|32). This is a simple estimation, since the source parameters are not exactly the same as the ones listed in Table I.

The actual contribution from each pair of modes is plotted in Fig. 4, where we show the squared SNR contribution for each pair of modes for the full IMR signal of our example source. Both axis correspond to the modes, so that the intersection represents the pair of modes ($lm|l'm'$). In the diagonal of the matrix we find

TABLE IV: Bayes factor for all models compared to the injected model

Bayes factor	Noiseless data set	Noisy data set
$\log(\mathcal{Z}_1/\mathcal{Z}_6)$	-6845	-6873
$\log(\mathcal{Z}_2/\mathcal{Z}_6)$	-976	-1015
$\log(\mathcal{Z}_3/\mathcal{Z}_6)$	-237	-259
$\log(\mathcal{Z}_4/\mathcal{Z}_6)$	-109	-134
$\log(\mathcal{Z}_5/\mathcal{Z}_6)$	-84	-100



FIG. 4: Final value of squared SNR of each pair of modes ($lm|l'm'$) for our example. Note the positive values for the square terms as well as the graduated values in the diagonal. In contra-position, note the negative values for pairs with different ‘m’ with the exception of cross terms (22|21) and (44|32). An interesting result is the relatively high value of (22|21), which is the second highest value.

the square terms, while in the upper and lower triangle we encounter the symmetric cross terms. The value in each box indicates the squared SNR of each pair, whose absolute value is shown by the colour bar. We can observe that the pair (22|22) indeed accounts for the largest contribution as expected, followed by the pairs (22|21), (33|33) and (22|33). The colour degradation when descending in the diagonal line is a consequence of the hierarchic ordering of modes. One striking difference with Fig.3 is the high contribution of (22|21) when compared to (33|33), showing that the details of the mode contributions will vary for different sources with different intrinsic and extrinsic parameters.

Even if the final value of a mode’s SNR is small for the complete IMR signal, it does not mean that its impact is negligible in relative terms everywhere in frequency, in particular in the pre-merger phase. This feature can be observed in Fig. 5, where we represent the absolute value of the squared SNR with respect to the frequency. The pairs contributions are separated in groups to make the

figures readable. We can see how some terms dominate in their group until a frequency that approximately corresponds to the merger, after which they later decrease. This happens for example for the pair (22|32) in the top right figure or (21|32) in the bottom left figure. Thus, statements about the relative importance of modes will depend in general on the termination frequency.

To quantify our ability to identify the presence of modes we use `dynesty` to compute the Bayes factor comparing all the models M_k with $k = 1, \dots, 5$ with M_6 . The results, written in Table IV, show clear negative values for all of them. This means that the model with 6 modes is preferred, and describes the data better than all of the other models, as expected. Even the value of -84 (-100 with noise) shows a significant predilection for the model M_6 over M_5 , where only the mode (4, 3) is absent. Thus, even the weakest modes in our settings should be identified as present in the data, which indicates that LISA observations will be capable of identifying waveform modes beyond the ones available in our current waveform models. If needed be, this advocates again for the use of waveforms with all available higher harmonics to capture all the physics in LISA signals, and for the further development of waveforms with higher mode contents. However, whether ignoring these weaker higher modes would produce biased parameter estimation results is another question, which we address in the following section.

C. Posterior and parameter bias

To assess the impact of the mode’s contribution on the estimation of the parameters, we show in Fig. 6 the posterior distribution of the logarithm of the chirp mass $\log M_c$, the mass ratio q and individual adimensional spins χ_1, χ_2 . Note that these parameters are relevant to the description of the remnant BH (see Section I and [18, 25]). The complete array of parameter’s posterior distribution can be found in Fig 12 in Appendix A.

We show four models out of the six models for comparison. The true values are represented by intersected black lines and the results from each model are distinguished by the colour code indicated in the legend. The parameter estimation for the model with only the quadrupolar mode (green colour) shows its deficiency in finding the true values, leading to biased estimations. In contrast with this result, the posterior of model M_6 (in blue) is centred on the true value for all parameters, as expected since the signal is injected and recovered with the same model. The models with 3 and 4 modes (M_3 and M_4 , orange and pink respectively) are also incorporated to highlight the better estimation of spin parameters when the mode (2, 1) is included in the waveform description (model M_4). This observation is consistent with the large relative contribution of (22|21) indicated by Fig. 4. The explanation of the importance of the (2, 1) mode, as well as the question whether this is generic or specific to our example source, are left for future investigations.

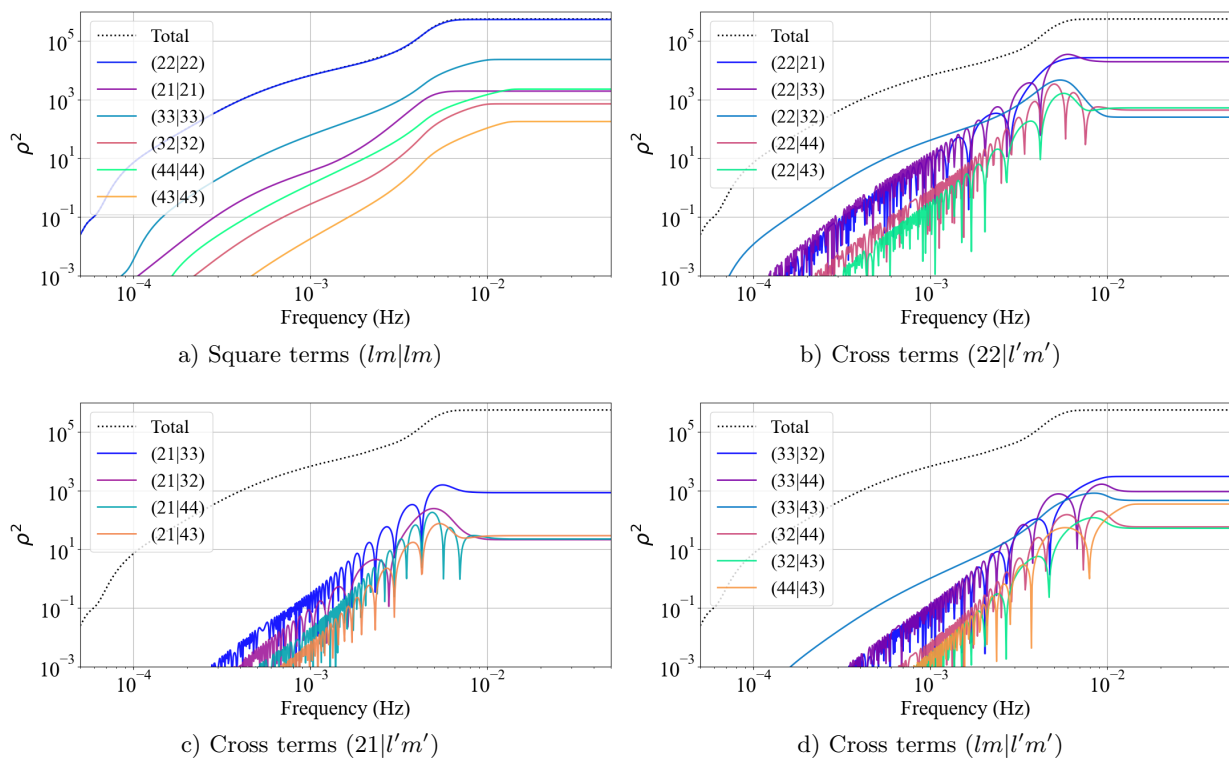


FIG. 5: Cumulative contribution to the squared SNR (in absolute value) of different pairs of modes depending on the frequency. The upper left figure shows the contribution of the square pairs, where we can see the quadrupolar making the higher contribution. All the other figures show cross terms, from where we can highlight the contribution of the quadrupolar mode with higher modes ($22|l'm'$), which are predominant over others cross terms.

TABLE V: Estimated value for models M_1 and M_6 , for the two data sets, without and with noise.

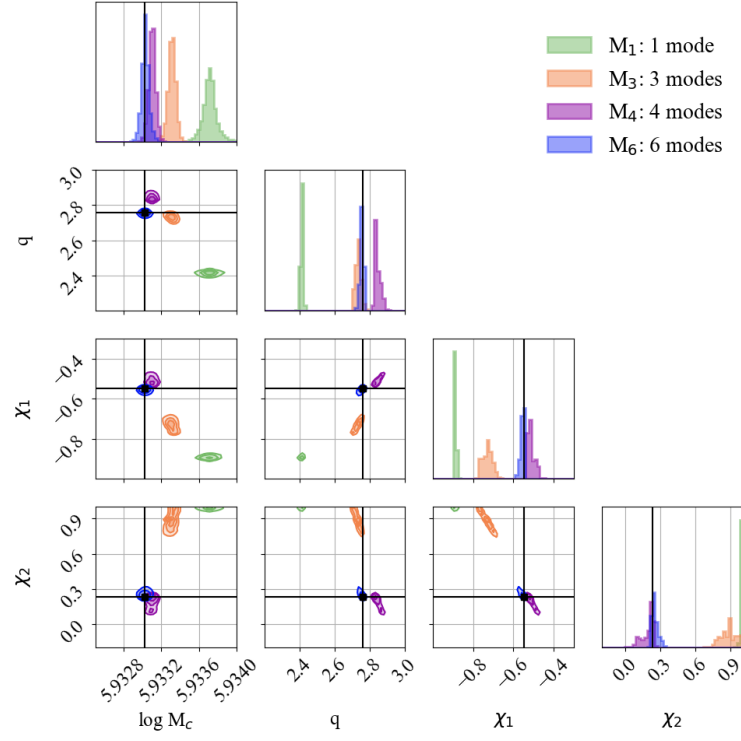
Parameter	True value	Estimated value with M_1 (noiseless)	Estimated value with M_6 (noiseless)	Estimated value with M_1 (with noise)	Estimated value with M_6 (with noise)
$\log M_c (M_\odot)$	5.93302	$5.93371^{+0.00019}_{-0.00016}$	$5.93303^{+0.00010}_{-0.00010}$	$5.93374^{+0.00019}_{-0.00016}$	$5.93304^{+0.00009}_{-0.00010}$
q	2.759	$2.411^{+0.012}_{-0.011}$	$2.751^{+0.019}_{-0.021}$	$2.414^{+0.012}_{-0.012}$	$2.759^{+0.013}_{-0.023}$
χ_1	-0.549	$-0.890^{+0.009}_{-0.007}$	$-0.559^{+0.016}_{-0.024}$	$-0.888^{+0.009}_{-0.008}$	$-0.549^{+0.011}_{-0.021}$
χ_2	0.232	$0.996^{+0.004}_{-0.019}$	$0.261^{+0.064}_{-0.043}$	$0.996^{+0.004}_{-0.018}$	$0.231^{+0.057}_{-0.030}$

In Table V we list the parameter's true values and the estimated values, with models M_1 and M_6 with and without the presence of noise. The super- and sub-scripts indicate the 68% confidence interval. We can see that in both cases, i.e. with and without noise, the model featuring only the dominant quadrupole mode is inaccurate in finding the true values, while the estimated mean value with all modes is consistent with the true value. This shows that for the medium-SNR and medium-mass case that we study (see Fig.4), the absence of higher modes would already result in biased estimated values. These biases would only get worse for higher-SNR and higher-mass systems.

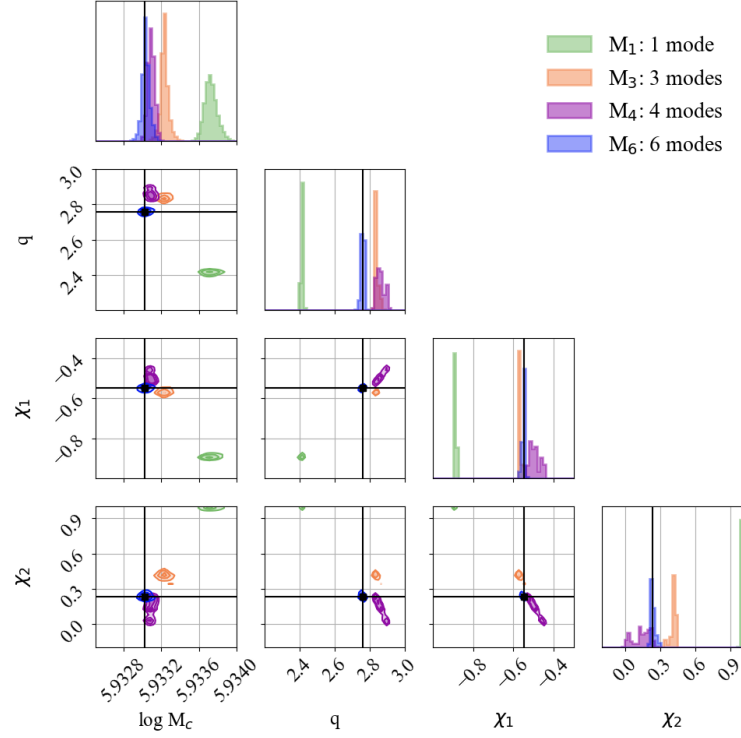
In Fig. 7 we illustrate the impact of the parameter biases on the reconstruction of post-merger waveform. Shown in Fig. 7a, we randomly select 200 samples from posterior distributions obtained with models M_1 , M_3 and

M_6 , and generate the waveform in the time domain with the same model. This illustration serves as a visual representation of the amplitude and phase from the results obtained by each model. The fact that we cannot distinguish individual lines is an effect of the small statistical errors: the posteriors are centred around biased parameters, but with a small dispersion. The waveform reconstruction would therefore be “confidently wrong”. Trying to inform a ringdown analysis with IMR information from biased analyses would presumably raise issues. If we compare M_3 and M_6 (in orange and blue respectively), enlarging the image we see visible differences in the post-merger. This feature, consistently with the significant Bayes factor for model M_6 over model M_3 , highlights the contribution of less predominant modes such as (2,1), (3,2) and (4,3).

In one of the tests performed to look for deviations

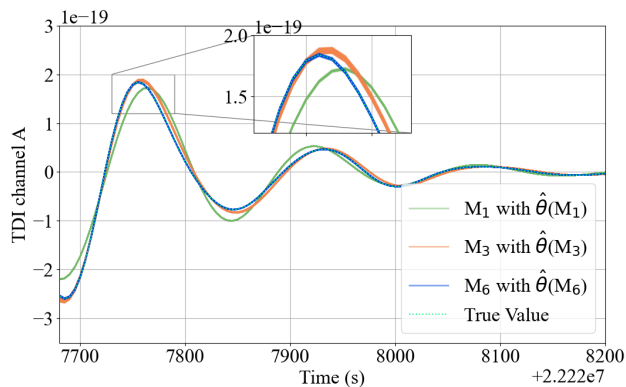


a) Marginalised posterior distribution on mass and spin parameters without noise.

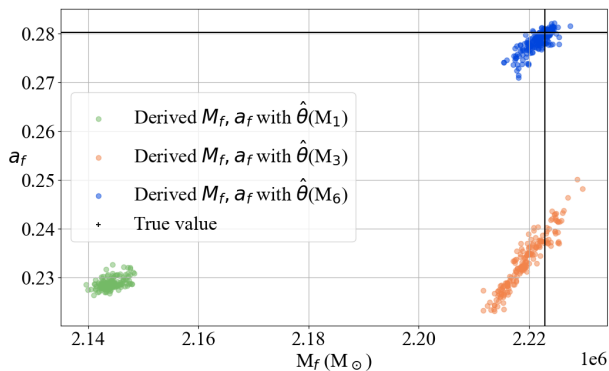


b) Marginalised posterior distribution on mass and spin parameters for noisy data.

FIG. 6: Four out of six models with different number of modes are represented here. The posterior of the model M_6 in blue manages to find the true values with high accuracy, while other models tend to induce biases, specially for spin parameters. In the bottom figure, we see how the introduction of noise does not change our ability to find the true values with 6 modes for this particular source.



a) Waveform obtained with models M_1 , M_3 and M_6 with parameters sampled from posterior distributions of the corresponding model.



b) Derived final mass and spin with posteriors from M_1 , M_3 and M_6 and the true value.

FIG. 7: Illustrative effect of biased parameters in the ringdown. In the top left figure, we see waveforms generated with the same model as the one used in the inference, obtained from 200 posterior samples for three models $\hat{\theta}(M_{1,3,6})$. We can see the consistency of the models with the injection, albeit its parameter bias. In the top right figure, we show the mass and spin of the remnant BH derived from each set of parameters (colored dots) and the true value (crossing black lines). This is a visual representation of the impact of biased parameter on the ringdown.

from GR in ringdown signals, on one hand one infers the final mass and spin from the ringdown signal, and on the other hand one derives these final mass and spin from the IMR posteriors with the help of formulas fitted on numerical relativity; the consistency between the two is the focus of the test. We do not perform a ringdown analysis here, but we illustrate in Fig. 7b how the parameter biases found in our IMR parameter estimation would translate into erroneous values when using posteriors to compute a derived final mass and spin, using the same fitted formulas as in PhenomHM [20] (see Eqs.(3.6) to (3.8) in [18]). We find that the IMR parameter biases

would indeed translate into significantly biased M_f and a_f as well, including the model M_3 .

D. Modelling error and SNR dependency

The magnitude of the bias on each parameter depends on the SNR and on the template waveform used for the inference, hence on the model M_k (with $k = 1, \dots, 6$). To properly analyze this issue, we introduce some definitions. Within the Fisher approximation, valid in principle in the high-SNR limit, the statistical error in each parameter σ_θ produced by the noise for a given waveform is determined as

$$\sigma_{\theta_i} = \sqrt{\Gamma_{ii}^{-1}}, \quad (27)$$

where $\Gamma_{ij} = \left(\frac{\partial h}{\partial \theta_i} \middle| \frac{\partial h}{\partial \theta_j} \right)$ is the Fisher information matrix. In this approximation, the statistical error scales directly as SNR^{-1} when keeping all parameters fixed (and adjusting the distance of the source to change the SNR). The bias $\Delta\theta(M_k)$ or “modelling error” due to the use of an incorrect template is defined as [59]

$$\Delta\theta_i = \hat{\theta}_i^0 - \hat{\theta}_i^{\text{temp}} = \sum_j \Gamma_{ij}^{-1}(\theta_k) \left(\frac{\partial h_k}{\partial \theta_j} \middle| \delta h_k \right), \quad (28)$$

where k correspond to models M_k , with $k = 1, \dots, 5$ and $\delta h_k = h_0 - h_k$ is the difference between the true waveform and the template waveform with model M_k . In our case, the template model corresponds to waveforms generated with the modes defined in Table III, so δh_k is simply the sum of the modes that were ignored.

As long as the statistical error σ_θ is larger than the error produced by the use of an incorrect template $\Delta\theta(M_k)$, with $k = 1, \dots, 5$, one can consider that the bias is irrelevant. On the contrary, if the statistical error is smaller than the modelling error, the waveform model is not sufficiently accurate to describe the data and the bias becomes relevant.

We first check in Fig. 8 whether the bias observed in the posterior distributions is consistent with the value obtained from the approximate Fisher bias formula Eq.(28). For intrinsic parameters, we show the bias from each model (black dot) and the error distribution obtained from the sampler (in colours). In the case of M_1 , we observe that the Fisher bias is much larger than the one found by sampling for all parameters, thus not appearing in the plot. Nevertheless, note that adimensional spins are limited to the interval $[-1, 1]$ in the sampler, while they are unconstrained in the Fisher matrix. In the case of M_2 the opposite happens and the posterior distribution exhibits a slightly larger error than the bias predicted by the Fisher analysis. Overall, from model M_3 to M_6 both errors become more and more consistent as parameter biases shrink. The same analysis for extrinsic parameters gave disagreeing results, with typically an overestimation of the Fisher bias compared to

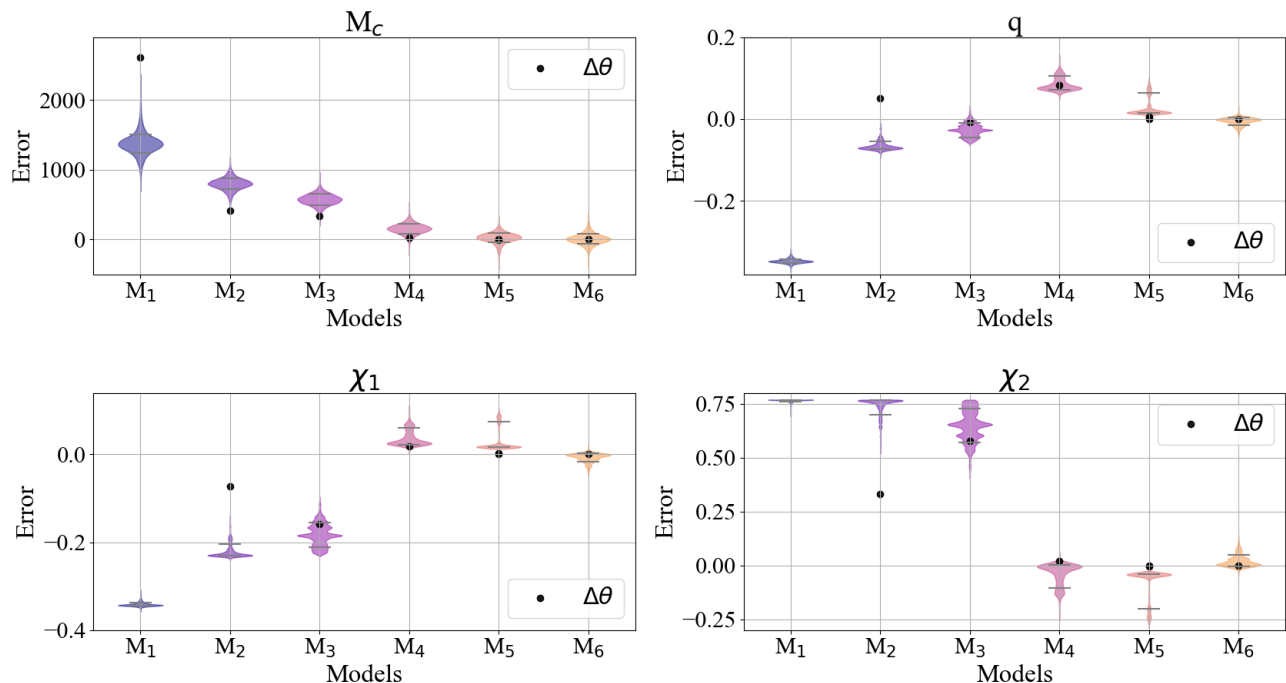


FIG. 8: Comparison of the error in the posterior distribution for all models (M_k , $k = 1, \dots, 6$ in colour) and modelling error (in black) for all parameters. The Fisher bias for M_1 in the spins and mass ratio lays outside of the plot given its large value. We see consistency between both errors in models M_k with $k = 3, 4, 5, 6$ as the bias decreases.

the posteriors. This could be due to degeneracies between parameters affecting the Fisher computation. The numerics of Fisher matrices are notoriously delicate and we leave this discrepancy for future investigation.

A natural question that arises is about the minimum SNR at which higher modes become important in parameter estimation. In other words, given a certain SNR, how many modes do we need to properly describe the waveform? One way to answer this question is by comparing the approximate statistical error for each parameter σ_θ with the systematic bias induced by an incorrect model $\Delta\theta(M_k)$. We perform this comparison in Fig. 9, where we show the errors for the intrinsic parameters with respect to the SNR. Varying the SNR amounts to changing the value of the luminosity distance D_L , leaving all other parameters unchanged. The Fisher bias in models M_1 and M_2 are not consistent with posteriors, as observed in Fig. 8. For this reason we will not discuss them, although they are plotted in the figure. The black diagonal line correspond to the statistical error in the model parameters (σ_θ) and the colour lines represent the modelling error produced by the wrong waveform template (M_k). With the same colour code as the modelling error, we mark in dotted lines the value of SNR at which the modelling error becomes higher than the statistical error.

For the chirp mass, in Fig. 9's top left panel, we see that the model M_3 (in pink) which includes modes (2, 2), (3, 3) and (4, 4) cannot describe well the data for sources with $\text{SNR} \geq 129$, since the bias becomes larger than the statistical error. Similarly, the model M_4 is sufficient

until the SNR reaches the value of 189 and M_5 until 984. Since the SNR of the source we consider in this work is around 744, the value of the chirp mass inferred with the model M_5 (in yellow) should be within the estimated error. However, to accurately infer the other parameters, the model M_5 works until a SNR of 107 for the mass ratio, until 156 for χ_1 and until 215 for χ_2 . Then, with an SNR of 744, this model will correctly estimate the chirp mass but will bias all the other parameters. For consistency, we checked the inferred values from the Bayesian analysis with M_5 and we confirm this statement.

This analysis does not put a limit on the number of modes needed to describe an event observed by LISA, but provides maximum SNR values to correctly estimate the parameters with a given model if less than these 6 modes are present in the waveform. Extrapolating from our example, we find that generically for sources detected by LISA with SNR of hundreds, we will have to make use of waveforms with at least 6 modes to properly estimate all intrinsic parameters. Note that the Fisher error in Eq.(27) and its scaling with SNR^{-1} are only approximate and are best valid for high SNRs and non-degenerate posteriors, so that our estimate does not replace a full parameter estimation study.

VI. CONCLUSIONS

We studied the contribution of IMR higher modes of a SMBHB source to the total SNR. We observed how

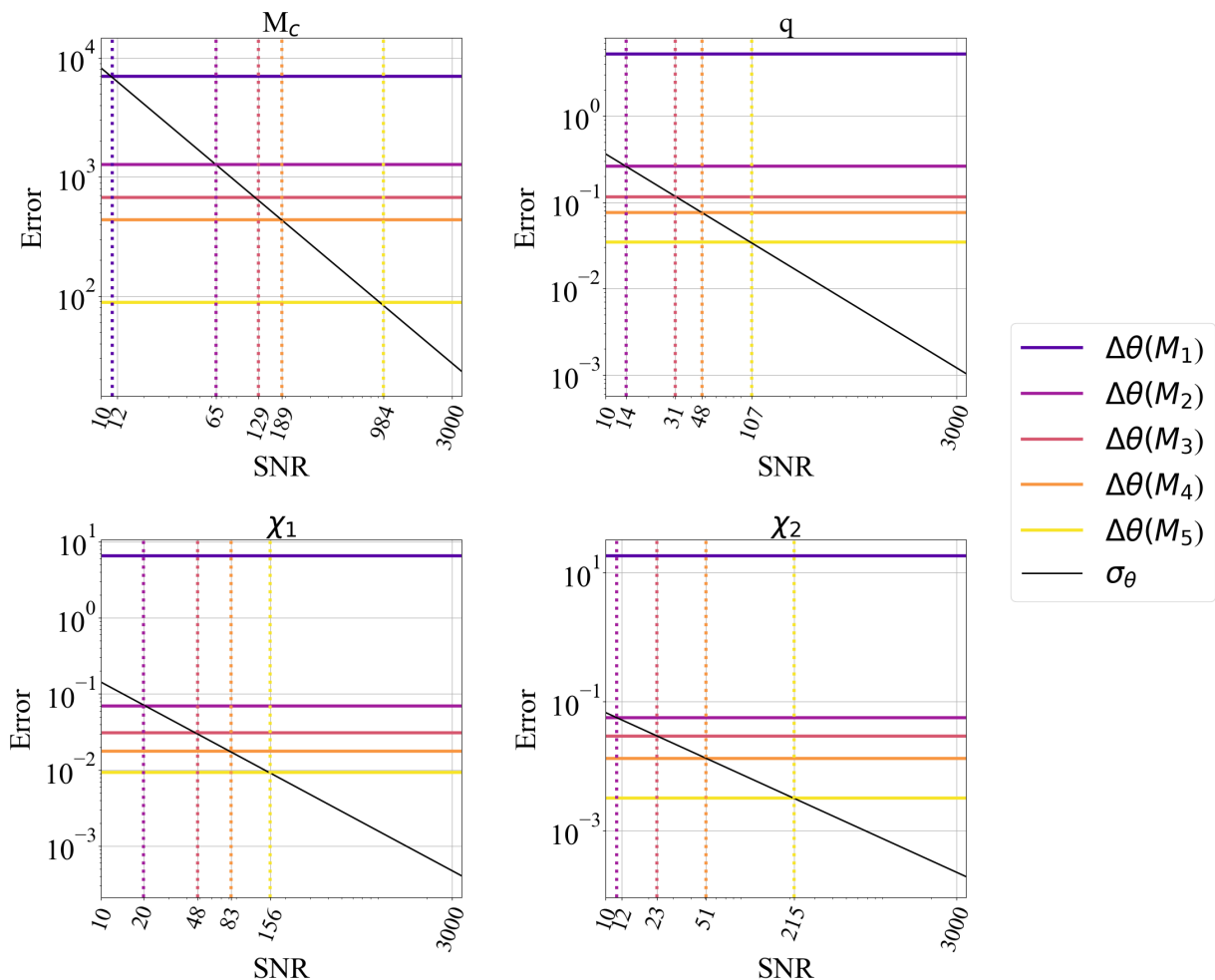


FIG. 9: Comparison of the statistical error (in black) and modelling errors (in colours) for relevant parameters in function of the SNR. When the statistical error becomes smaller than the modelling error, that model does no longer fit well the data and bias the estimated parameters. The SNR for this transition is marked with dotted lines in the correspondent colour for each incorrect template (models M_k , $k = 1, \dots, 5$).

this contribution depends on the redshifted mass of the event through the frequency, which is directly related to LISA’s response and sensitivity. We also showed that the cross terms could act as constructive or destructive contributions to the total SNR, depending on the signal frequency and observational parameters. We presented a map guide of the relevance of each mode given the mass of an event. We highlighted the role of higher modes in SMBHB with masses of the order of $10^8 M_\odot$. In LISA, large mass sources enhance the contribution of modes with higher frequencies. Consequently, the quadrupolar mode will no longer dominate in these heavy sources in LISA.

We defined different models, each including different harmonics to compare sensitivity performances. We could distinguish higher modes by comparing the Bayesian evidence for different models. In our example of a noisy signal with six modes, the model M_6 , which includes the same higher modes as in the injection, was the

preferred one, as expected. The model M_6 showed a very significant Bayes factor compared to models with fewer modes. Furthermore, we found that the absence of modes in the waveform template can bias the parameter estimation for high SNR sources due to the non-orthogonality of the modes in the merger-ringdown phase. Biased binary parameters can lead to a biased inference of the remnant BH’s mass and spin. This effect can corrupt the No-hair theorem test and lead to misinterpretations.

We could quantify the SNR needed to distinguish models by comparing statistical errors of the injected waveform parameters with the modelling errors produced using an incorrect template (M_k , $k = 1, \dots, 5$). In other words, given a certain SNR, we can specify the modes needed to infer the parameters without significant bias. This quantification depends on the actual waveform, which includes six modes in our analysis. In reality, such a situation is unlikely, as we expect more modes in the dynamics. Hence, in this study, we have not set a limit

on the number of observable modes, which is still an open question that can be answered once more harmonics are implemented. However, our work demonstrates the need for higher modes in the waveform templates to perform accurate GW source characterization with LISA. Besides, featuring precession and eccentricity will also be necessary.

The ability of LISA to identify different modes allows us to consider GR tests on more solid grounds, including the test of the No-hair theorem, which will be the subject of a forthcoming study.

ACKNOWLEDGMENTS

This work was supported by CNES, focused on LISA Mission. We gratefully acknowledge support from the CNRS/IN2P3 Computing Center (Lyon - France) for providing computing and data-processing resources needed

for this work. CP acknowledges financial support from CNES Grant No. 51/20082 and CEA Grant No. 2022-039.

Appendix A: Complementary results

To assess how the mass ratio affects the SNR, we show in Fig. 10 the contour plots for mass ratio versus total source mass for a source with parameters given in Table II and redshift $z = 2$. The absence of contribution at leading PN order of modes with odd m for equal mass ratio (see e.g.[60]) is illustrated here. We can also note the importance of higher modes for sources with a mass around $10^6 M_\odot$ and mass ratio between 2 and 15.

For completeness, we also include here the square and cross terms of the SNR contributions from Section IV B. As well as the marginalised posterior on all parameters for M_1 , M_3 and M_6 with noisy data from Section V C.

-
- [1] P. Amaro-Seoane *et al.*, Laser Interferometer Space Antenna, arXiv e-prints , arXiv:1702.00786 (2017), arXiv:1702.00786 [astro-ph.IM].
 - [2] LISA Science Study Team, *LISA Science Requirements Document*, Requirement Document ESA-L3-EST-SCIRS-001-i1.0 (ESA, 2018) <https://www.cosmos.esa.int/web/lisa/lisa-documents/>.
 - [3] P. Amaro-Seoane *et al.*, Astrophysics with the laser interferometer space antenna (2022).
 - [4] A. Sesana, Black Hole Science With the Laser Interferometer Space Antenna, *Front. Astron. Space Sci.* **8**, 601 (2021), arXiv:2105.11518 [astro-ph.CO].
 - [5] B. Carter, Axisymmetric black hole has only two degrees of freedom, *Phys. Rev. Lett.* **26**, 331 (1971).
 - [6] O. Dreyer, B. Kelly, B. Krishnan, L. S. Finn, D. Garrison, and R. Lopez-Aleman, Black-hole spectroscopy: testing general relativity through gravitational-wave observations, *Classical and Quantum Gravity* **21**, 787 (2004).
 - [7] W. H. Press and S. A. Teukolsky, Perturbations of a Rotating Black Hole. II. Dynamical Stability of the Kerr Metric, *The Astrophysical Journal* **185**, 649 (1973).
 - [8] S. Chandrasekhar and S. Detweiler, The quasi-normal modes of the schwarzschild black hole, *Proceedings of the Royal Society of London. A. Mathematical and Physical Sciences* **344**, 441 (1975), <https://royalsocietypublishing.org/doi/pdf/10.1098/rspa.1975.0112>.
 - [9] H.-P. Nollert, Quasinormal modes: the characteristic ‘sound’ of black holes and neutron stars, *Classical and Quantum Gravity* **16** (1999).
 - [10] K. D. Kokkotas and B. G. Schmidt, Quasi-normal modes of stars and black holes, *Living Reviews in Relativity* **2**, 10.12942/lrr-1999-2 (1999).
 - [11] F. Echeverria, Gravitational-wave measurements of the mass and angular momentum of a black hole, *Phys. Rev. D* **40**, 3194 (1989).
 - [12] E. Berti, V. Cardoso, and C. M. Will, Gravitational-wave spectroscopy of massive black holes with the space interferometer LISA, *Physical Review D* **73**, 10.1103/physrevd.73.064030 (2006).
 - [13] I. Kamaretsos, M. Hannam, S. Husa, and B. S. Sathyaprakash, Black-hole hair loss: Learning about binary progenitors from ringdown signals, *Physical Review D* **85**, 10.1103/physrevd.85.024018 (2012).
 - [14] I. Kamaretsos, M. Hannam, and B. S. Sathyaprakash, Is black-hole ringdown a memory of its progenitor?, *Physical Review Letters* **109**, 10.1103/physrevlett.109.141102 (2012).
 - [15] E. Berti and A. Klein, Mixing of spherical and spheroidal modes in perturbed kerr black holes, *Physical Review D* **90**, 10.1103/physrevd.90.064012 (2014).
 - [16] L. London, D. Shoemaker, and J. Healy, Modeling ringdown: Beyond the fundamental quasinormal modes, *Physical Review D* **90**, 10.1103/physrevd.90.124032 (2014).
 - [17] B. J. Kelly and J. G. Baker, Decoding mode mixing in black-hole merger ringdown, *Physical Review D* **87**, 10.1103/physrevd.87.084004 (2013).
 - [18] S. Husa, S. Khan, M. Hannam, M. Pürrer, F. Ohme, X. J. Forteza, and A. Bohé, Frequency-domain gravitational waves from nonprecessing black-hole binaries. i. new numerical waveforms and anatomy of the signal, *Phys. Rev. D* **93**, 044006 (2016).
 - [19] S. Khan, S. Husa, M. Hannam, F. Ohme, M. Pürrer, X. J. Forteza, and A. Bohé, Frequency-domain gravitational waves from nonprecessing black-hole binaries. ii. a phenomenological model for the advanced detector era, *Phys. Rev. D* **93**, 044007 (2016).
 - [20] L. London, S. Khan, E. Fauchon-Jones, C. García, M. Hannam, S. Husa, X. Jiménez-Forteza, C. Kalaghatgi, F. Ohme, and F. Pannarale, First higher-multipole model of gravitational waves from spinning and coalescing black-hole binaries, *Physical Review Letters* **120**, 10.1103/physrevlett.120.161102 (2018).
 - [21] S. Marsat and J. G. Baker, Fourier-domain modulations and delays of gravitational-wave signals (2018).
 - [22] S. Gossan, J. Veitch, and B. S. Sathyaprakash, Bayesian model selection for testing the no-hair theorem with black hole ringdowns, *Physical Review D* **85**, 10.1103/phys-

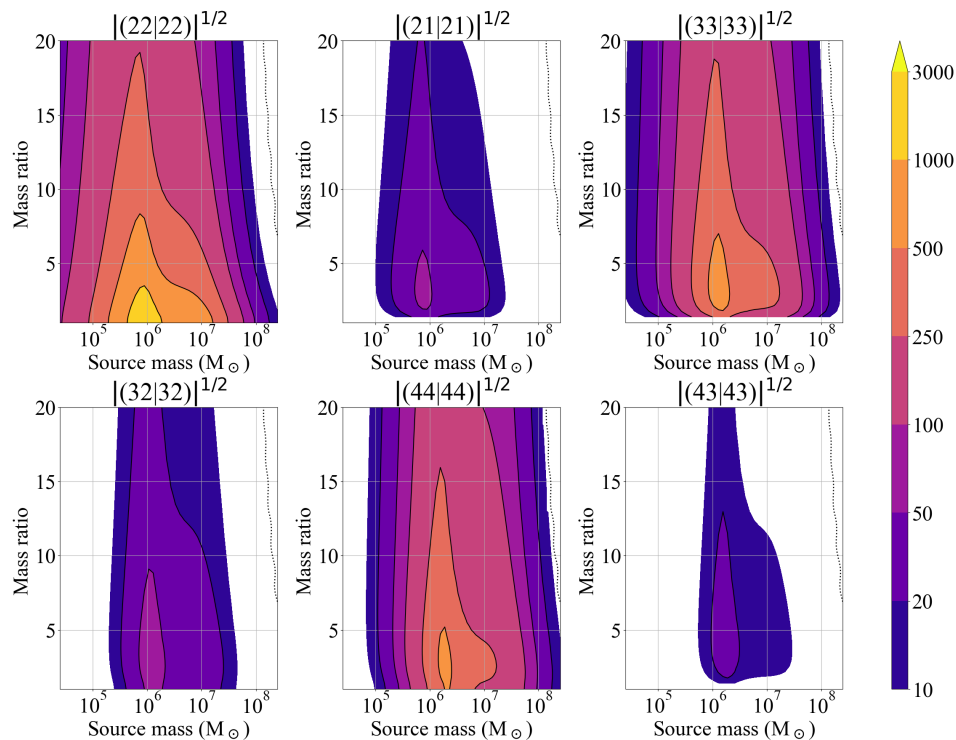


FIG. 10: Contour plot for mass ratio with respect to the mass. We remark the contribution of higher modes for sources of $\sim 10^6 M_\odot$ and mass ratios up to 15. Also note the slow reduction of SNR when increasing the mass ratio by a few unities for the same masses.

- revd.85.124056 (2012).
- [23] B. P. Abbott and others. (LIGO Scientific and Virgo Collaborations), Tests of general relativity with gw150914, *Phys. Rev. Lett.* **116**, 221101 (2016).
- [24] S. Bhagwat and C. Pacilio, Merger-ringdown consistency: A new test of strong gravity using deep learning, *Physical Review D* **104**, 10.1103/physrevd.104.024030 (2021).
- [25] Y. Pan, A. Buonanno, M. Boyle, L. T. Buchman, L. E. Kidder, H. P. Pfeiffer, and M. A. Scheel, Inspiral-merger-ringdown multipolar waveforms of nonspinning black-hole binaries using the effective-one-body formalism, *Physical Review D* **84**, 10.1103/physrevd.84.124052 (2011).
- [26] E. Berti, V. Cardoso, and A. O. Starinets, Quasinormal modes of black holes and black branes, *Classical and Quantum Gravity* **26**, 163001 (2009).
- [27] V. Baibhav and E. Berti, Multimode black hole spectroscopy, *Physical Review D* **99**, 10.1103/physrevd.99.024005 (2019).
- [28] V. Baibhav, E. Berti, and V. Cardoso, LISA parameter estimation and source localization with higher harmonics of the ringdown, *Physical Review D* **101**, 10.1103/physrevd.101.084053 (2020).
- [29] M. Giesler, M. Isi, M. A. Scheel, and S. A. Teukolsky, Black hole ringdown: The importance of overtones, *Physical Review X* **9**, 10.1103/physrevx.9.041060 (2019).
- [30] S. Bhagwat, X. J. Forteza, P. Pani, and V. Ferrari, Ringdown overtones, black hole spectroscopy, and no-hair theorem tests, *Physical Review D* **101**, 10.1103/physrevd.101.044033 (2020).
- [31] E. Thrane, P. D. Lasky, and Y. Levin, Challenges for testing the no-hair theorem with current and planned gravitational-wave detectors, *Physical Review D* **96**, 10.1103/physrevd.96.102004 (2017).
- [32] J. Meidam, M. Agathos, C. V. D. Broeck, J. Veitch, and B. Sathyaprakash, Testing the no-hair theorem with black hole ringdowns using TIGER, *Physical Review D* **90**, 10.1103/physrevd.90.064009 (2014).
- [33] R. Abbott and others. (LIGO Scientific Collaboration and Virgo Collaboration), Tests of general relativity with binary black holes from the second ligo-virgo gravitational-wave transient catalog, *Phys. Rev. D* **103**, 122002 (2021).
- [34] M. Isi, M. Giesler, W. M. Farr, M. A. Scheel, and S. A. Teukolsky, Testing the no-hair theorem with GW150914, *Physical Review Letters* **123**, 10.1103/physrevlett.123.111102 (2019).
- [35] J. C. Bustillo, P. D. Lasky, and E. Thrane, Black-hole spectroscopy, the no-hair theorem, and GW150914: Kerr versus occam, *Physical Review D* **103**, 10.1103/physrevd.103.024041 (2021).
- [36] G. Carullo, W. D. Pozzo, and J. Veitch, Observational black hole spectroscopy: A time-domain multimode analysis of GW150914, *Physical Review D* **99**, 10.1103/physrevd.99.123029 (2019).
- [37] C. D. Capano and A. H. Nitz, Binary black hole spectroscopy: A no-hair test of GW190814 and GW190412, *Physical Review D* **102**, 10.1103/physrevd.102.124070 (2020).
- [38] R. Cotesta, G. Carullo, E. Berti, and V. Cardoso, Analysis of ringdown overtones in GW150914, *Physical Review Letters* **129**, 10.1103/physrevlett.129.111102 (2022).

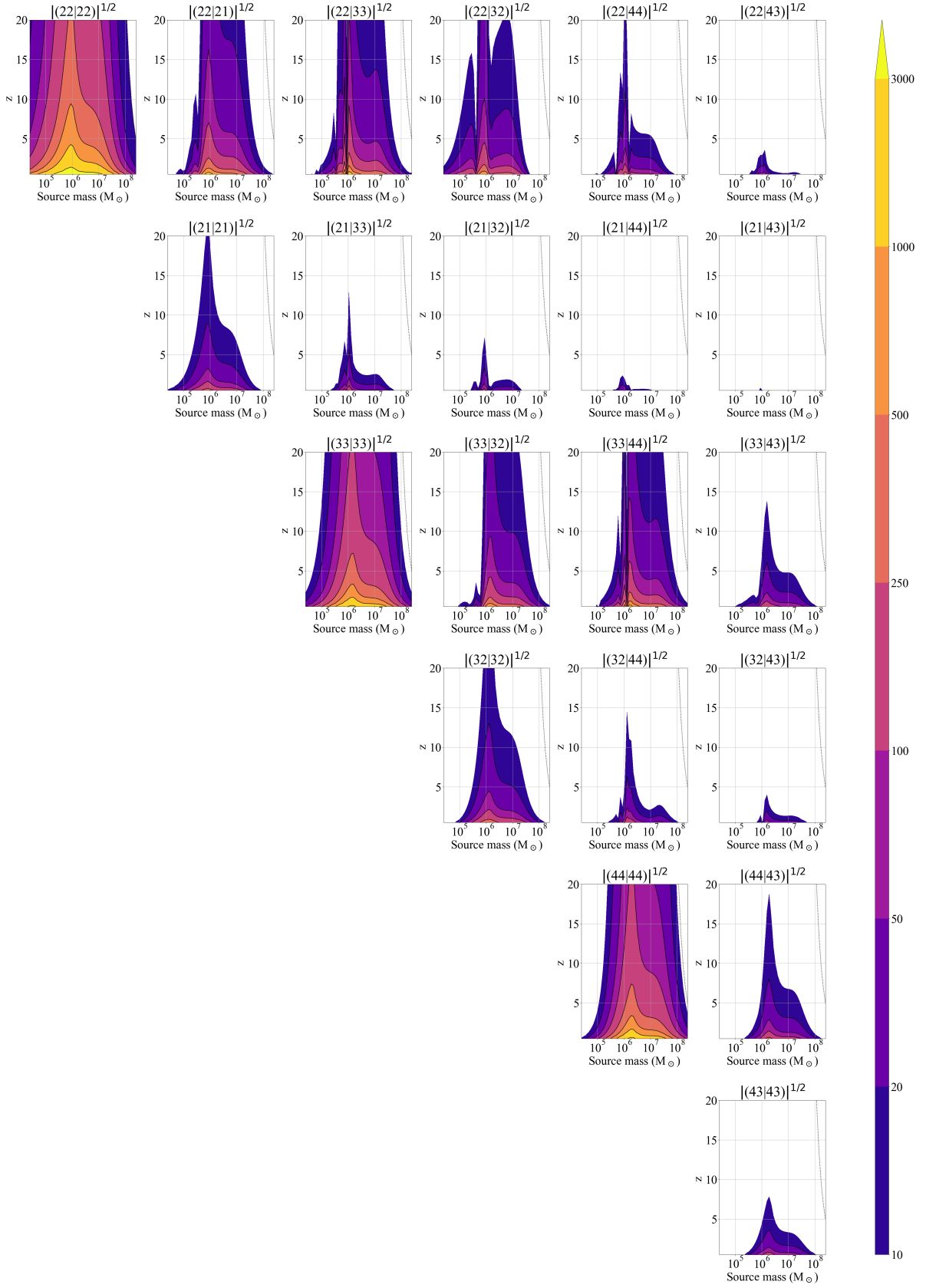


FIG. 11: SNR contribution for each pair of modes

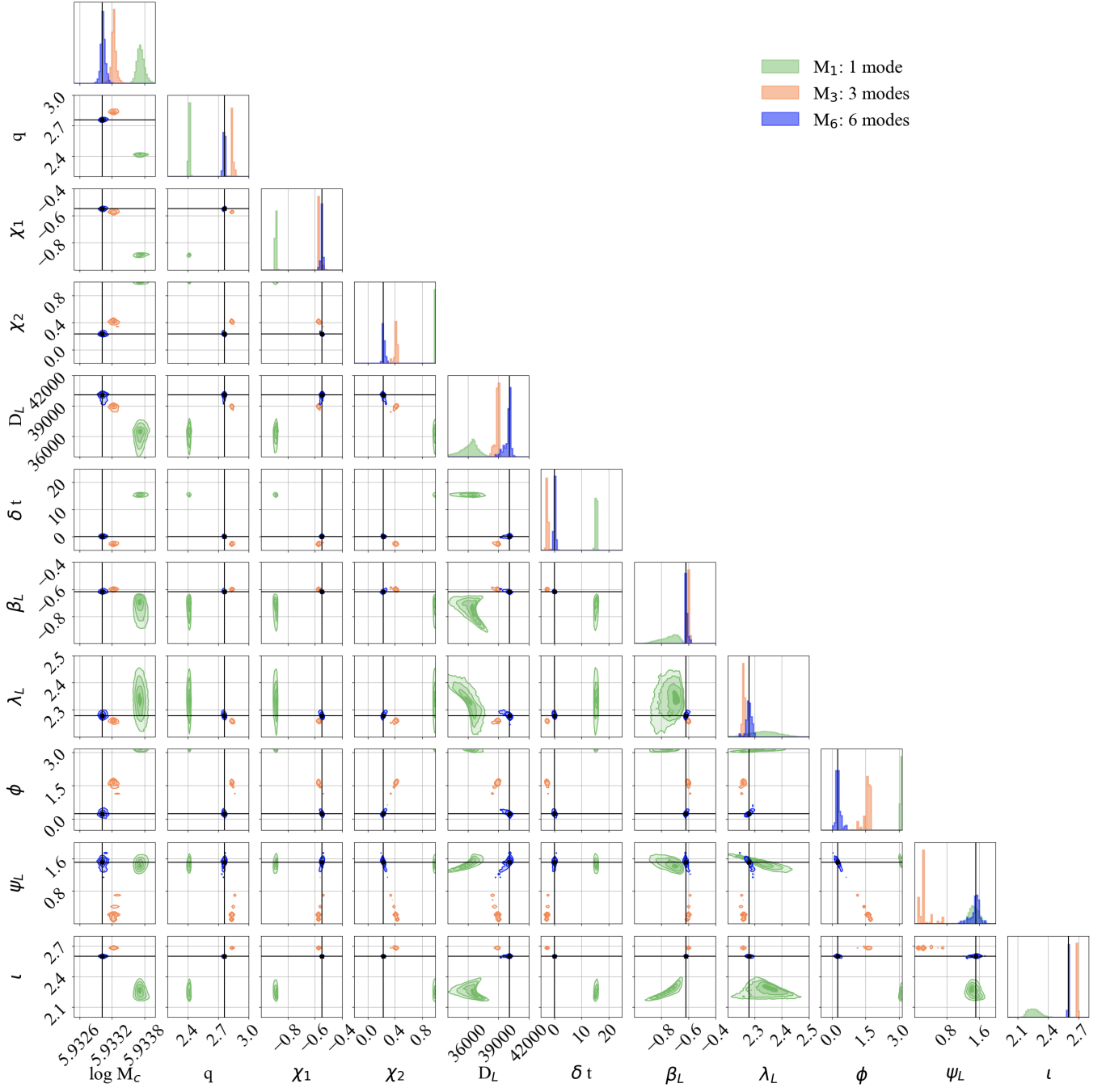


FIG. 12: Marginalised posterior distribution for all parameters. Here M_1 in green, M_3 in orange and M_6 in blue with true values represented with black lines. Note the high accuracy of the estimated mean value of all parameters found with the model M_6 .

- [39] B. P. Abbott and others. (LIGO Scientific Collaboration and Virgo Collaboration), Observation of gravitational waves from a binary black hole merger, *Phys. Rev. Lett.* **116**, 061102 (2016).
- [40] R. Brito, A. Buonanno, and V. Raymond, Black-hole spectroscopy by making full use of gravitational-wave modeling, *Physical Review D* **98**, 10.1103/physrevd.98.084038 (2018).
- [41] Lisabeta, for the moment only accessible for LISA Consortium members.
- [42] S. Marsat, J. G. Baker, and T. D. Canton, Exploring the bayesian parameter estimation of binary black holes with LISA, *Physical Review D* **103**, 10.1103/physrevd.103.083011 (2021).
- [43] G. Pratten, A. Klein, C. J. Moore, H. Middleton, N. Steinle, P. Schmidt, and A. Vecchio, On the lisa science performance in observations of short-lived signals from massive black hole binary coalescences (2022).
- [44] J.-B. Bayle, O. Hartwig, and M. Staab, Adapting time-delay interferometry for LISA data in frequency, *Physical Review D* **104**, 10.1103/physrevd.104.023006 (2021).
- [45] M. Tinto and J. W. Armstrong, Cancellation of laser noise in an unequal-arm interferometer detector of gravitational radiation, *Phys. Rev. D* **59**, 102003 (1999).
- [46] M. Vallisneri, Geometric time delay interferometry, *Phys. Rev. D* **72**, 042003 (2005), [Erratum: *Phys. Rev. D* **76**, 109903 (2007)], arXiv:gr-qc/0504145.
- [47] J. W. Armstrong, F. B. Estabrook, and M. Tinto, Time-delay interferometry for space-based gravitational wave searches, *The Astrophysical Journal* **527**, 814 (1999).
- [48] C. Cutler and É. E. Flanagan, Gravitational waves from merging compact binaries: How accurately can one extract the binary's parameters from the inspiral waveform?, *Physical Review D* **49**, 2658 (1994).
- [49] A. Klein, N. Cornish, and N. Yunes, Gravitational waveforms for precessing, quasicircular binaries via multiple scale analysis and uniform asymptotics: The near spin alignment case, *Physical Review D* **88**, 10.1103/physrevd.88.124015 (2013).
- [50] T. A. Prince, M. Tinto, S. L. Larson, and J. W. Armstrong, LISA optimal sensitivity, *Physical Review D* **66**, 10.1103/physrevd.66.122002 (2002).
- [51] E. Berti, V. Cardoso, J. A. Gonzalez, U. Sperhake, M. Hannam, S. Husa, and B. Brügmann, Inspiral, merger, and ringdown of unequal mass black hole binaries: A multipolar analysis, *Physical Review D* **76**, 10.1103/physrevd.76.064034 (2007).
- [52] S. Bhagwat, M. Okounkova, S. W. Ballmer, D. A. Brown, M. Giesler, M. A. Scheel, and S. A. Teukolsky, On choosing the start time of binary black hole ringdowns, *Physical Review D* **97**, 10.1103/physrevd.97.104065 (2018).
- [53] N. J. Cornish, Fast fisher matrices and lazy likelihoods (2010).
- [54] N. J. Cornish, Heterodyned likelihood for rapid gravitational wave parameter inference, *Physical Review D* **104**, 10.1103/physrevd.104.104054 (2021).
- [55] M. Le Jeune and S. Babak, Lisa data challenge sangria (ldc2a) (2022).
- [56] J. S. Speagle, DYNesty: a dynamic nested sampling package for estimating Bayesian posteriors and evidences, *Monthly Notices of the Royal Astronomical Society* **493**, 3132 (2020), arXiv:1904.02180 [astro-ph.IM].
- [57] W. D. Voursden, W. M. Farr, and I. Mandel, Dynamic temperature selection for parallel tempering in markov chain monte carlo simulations, *Monthly Notices of the Royal Astronomical Society* **455**, 1919 (2015).
- [58] D. Foreman-Mackey, D. W. Hogg, D. Lang, and J. Goodman, emcee: The MCMC hammer, *Publications of the Astronomical Society of the Pacific* **125**, 306 (2013).
- [59] C. Cutler and M. Vallisneri, LISA detections of massive black hole inspirals: Parameter extraction errors due to inaccurate template waveforms, *Physical Review D* **76**, 10.1103/physrevd.76.104018 (2007).
- [60] K. G. Arun, A. Buonanno, G. Faye, and E. Ochsner, Erratum: Higher-order spin effects in the amplitude and phase of gravitational waveforms emitted by inspiraling compact binaries: Ready-to-use gravitational waveforms [*phys. rev. d* **79**, 104023 (2009)], *Phys. Rev. D* **84**, 049901 (2011).